

Density profiles of oceanic slabs and surrounding mantle: Integrated thermodynamic and thermal modeling, and implications for the fate of slabs at the 660 km discontinuity

Jibamitra Ganguly^{a,*}, Andrew M. Freed^b, Surendra K. Saxena^c

^a Department of Geosciences, University of Arizona, Tucson, AZ, USA

^b Department of Earth and Atmospheric Sciences, Purdue University, West Lafayette, IN 47906, USA

^c CeSMEC, Center for the Study of Matter Under Extreme Condition, Florida International University, Miami, FL 33199, USA

ARTICLE INFO

Article history:

Received 7 February 2008

Received in revised form

30 September 2008

Accepted 9 October 2008

Keywords:

Density

Transition zone

Mantle

Slab

Subduction

ABSTRACT

We have calculated the mineralogical properties of the Earth's mantle and the lithological units constituting the subducting oceanic slabs within a wide range of P–T conditions within the CaO–FeO–MgO–Al₂O₃–SiO₂ system, except for the basalt top-layer of a slab, for which the system is extended to include Na₂O. The mineralogical data are then converted, using the appropriate P–V–T relations, to bulk densities. The calculated adiabatic density vs. depth profile of the mantle between 200 and 725 km depths is in good agreement with geophysical and experimental data. The density data of the different compositional units are combined with calculated thermal structures for a variety of slab–mantle systems to construct equilibrium density profiles as a function of depth. The mean equilibrium densities of the slabs within the transition zone (400–660 km depth) are found to be ~ 0.04 – 0.05 g/cm³ greater than those of the ambient mantle within the same depth interval. For the entire upper mantle, density differences between slabs and ambient mantle are slightly less, but the slabs still remain denser than the latter. At 670 km depth, slabs have lower density than the ambient lower mantle because of the commencement of perovskite forming reactions within the mantle, and displacements of these reaction boundaries to higher pressures within the slabs as a consequence of their negative P–T slopes. If perovskite forming reactions within slabs are hindered for kinetic sluggishness, then neutral buoyancy would be achieved when the slabs have penetrated ~ 100 km into the lower mantle. However, using the available data on the kinetics of spinel to perovskite plus periclase reaction, we conclude that the reaction would go to completion in a Peru-type young slab (41 Myr), and very likely also in a Tonga-type old slab (110 Myr), before these penetrated 100 km into the lower mantle. Thus, slabs should always remain negatively buoyant, and therefore continue to subduct through the lower mantle once it penetrates through the 660 km discontinuity. Despite a negative buoyancy force, a slab could deflect at the top of the lower mantle (660 km) because of factors resisting subduction, namely viscosity jump, low dip angle, slab roll back, and metastable persistence of olivine in cold slabs. If published scale model experiments represent realistic approximations of the factors affecting plate subduction, then according to our density data, any slab with a dip angle of ≤ 40 – 50° would bend at the 660 km discontinuity if there is a viscosity jump of at least by a factor of ~ 10 and trench migration. The basalt top-layer of a slab is denser than other slab components and the ambient mantle at all depths to 660 km, and therefore should continue to sink into the lower mantle, especially if a slab directly penetrates the 660 km barrier, instead of peeling off in the transition zone to form a “perched eclogite” or “piclogite” layer, as previously proposed. The harzburgite layer, which is sandwiched between denser basalt and lherzolite layers, faces greater resistance to subduction, especially in a young slab, and thus could significantly contribute to the deformation of a slab near the 660 km discontinuity.

© 2008 Elsevier B.V. All rights reserved.

1. Introduction

It is commonly accepted that the 660 (± 10) km deep seismic discontinuity in the Earth's mantle, which defines the top of lower mantle, is primarily due to the ringwoodite (Rng) to Mg-perovskite (MgPv) plus magnesiowüstite (Mg–Wu) transformation.

* Corresponding author. Tel.: +1 520 621 6006; fax: +1 520 621 2672.
E-mail address: ganguly@email.arizona.edu (J. Ganguly).

Experimental data between 1000 and 2000 °C show the P–T slope of this transition to be negative, with estimates varying between –30 bar/K (Ito and Takahashi, 1989) and –13(±3) bar/K (Katsura et al., 2003; Fei et al., 2004). Since the interior of a subducting oceanic slab is colder than the ambient mantle at the same depth, the negative P–T slope of the transition implies Rng to MgPv plus Mg–Wu transformation at a greater depth within a slab than in the ambient mantle. This has led to the idea that the density of the slab at ~660 km depth is lower than that of the ambient mantle, thereby opposing or even preventing the slab's descent into the lower mantle (e.g. Ringwood, 1994; Davies, 1999). Seismic tomographic images, however, show both deflection of slabs at the 660 km depth and penetration to greater depths (e.g. van der Hilst et al., 1991; Grand et al., 1997). Understanding of balance of forces that control the fate of subducting slabs at the top of the lower mantle requires a comprehensive analysis of the density structure taking into account the effects of all important phase transformations in the slab–mantle system, rather than only the effect of Rng to MgPv + Mg–Wu transformation. Davies (1999) called attention to the possibility that the effect of the Rng to MgPv + Mg–Wu transformation on the buoyancy force of a slab may be significantly counterbalanced by other phase transformations with positive P–T slopes, and thus emphasized the need for calculations in the multicomponent and multiphase system. Also, inasmuch as the primary driving force for plate subduction comes from the negative buoyancy force on slabs (e.g. Forsyth and Uyeda, 1975; Hager, 1984), a comprehensive analysis of the buoyancy force taking into account the effects of thermal structure and mineralogical reactions in systems, which closely approximate the natural systems, constitutes an important step in our understanding of the dynamics of plate motions.

Ringwood (1982) suggested that an oceanic slab of ~80 km thickness is lithologically stratified with an upper ~6 km of basalt, followed successively downward by ~24 km layer of residual harzburgite, ~10 km layer of residual lherzolite and ~40 km layer of slightly depleted pyrolite. The last three components represent the residues left after different degrees of partial melting of pyrolitic mantle rock and extraction of basalt, with harzburgite being the most refractory component. Hoffmann and White (1982) proposed that the basaltic crust of a slab has a greater density than the mantle throughout its entire depth, and consequently it should separate from the associated refractory lithosphere and sink, perhaps all the way to the core–mantle boundary, thereby forming a layer of “degenerate crust”. They envisioned this buried crustal layer to be the source of mantle plumes. Anderson (1989), on the other hand, suggested that the basaltic crust becomes lighter than the pyrolitic mantle at the 660 km discontinuity, and is thus trapped during subduction to form a “perched eclogite layer”. This viewpoint was later supported by Irifune and Ringwood (1993) on the basis of their experimental data and calculation of the zero pressure density (1 bar, 298 K) of the assemblages observed in their experimental products at high P–T condition. However, using results from *in situ* determination of mineralogical transformations in basalt, Litasov et al. (2005) concluded that there is no density cross-over between the basaltic component of a cold slab and surrounding mantle at the 660 km depth, and consequently, the basaltic component should penetrate into the lower mantle.

In this work, we have taken a computational thermodynamic approach to the problem of density structure of the slab–mantle system within and around the transition zone, and present the details of density variation within the different lithological components as a function of temperature at pressures corresponding to 200–800 km depth, rather than zero-pressure densities as in the most earlier studies. We also calculate the thermal structures of selected slabs, and integrate the data with the results of the thermodynamic calculations to develop a comprehensive understanding of

density variations within and around slabs of widely differing ages, vertical descent rates and subduction angles.

2. Thermodynamic calculations

2.1. Data and methodology

We take the compositions of the following rock types to represent the major element bulk chemistries of the different lithological units of an 80 km thick slab (Fig. 1): Grt–lherzolite from Kilborne Hole (KH), New Mexico (Takahashi, 1986), for the slightly depleted pyrolite (lowest 40 km) and residual lherzolite (10 km) layers, ophiolitic harzburgite (Brown and Mussett, 1981) for the residual harzburgite component, and the average between oceanic-basalt (Brown and Mussett, 1981) and mid-ocean ridge basalt (MORB; Ringwood and Irifune, 1988) for the top basalt layer of a slab. The major element compositional distinction between residual lherzolite and slightly depleted pyrolite is minor in terms of its effect on the density structures of these units. The bulk composition of the ambient mantle is assumed to be given by the average of three compositions, namely (a) the pyrolite model composition of Ringwood (1982), (b) mantle composition based on the assumption of average solar system abundance ratios for the whole Earth (Palme and O'Neill, 2003) and (c) composition of KLB-1 peridotite (Takahashi, 1986). The system CaO–FeO–MgO–Al₂O₃–SiO₂ (CFMAS) constitutes ~99 wt% of KH-lherzolite and ophiolitic harzburgite, ~98 wt% of assumed ambient mantle composition and ~95 wt% of the average of oceanic basalt and MORB. Thus, for the purpose of phase equilibrium calculations, the system CFMAS is considered to be an adequate representation of the major element compositional space of the different lithologic units, except for basalt. For the latter, we include Na₂O as an additional component. The Na₂O–CFMAS or NCFMAS constitutes ~97 wt% of the composition of the adopted basalt composition. All compositions are normalized within the respective subsystems, and summarized in Table 1. We mention at the outset that compositional variations within the proposed limits of the different lithologic units do not have any significant effect on the density structures of the slab–mantle system that are deduced below.

All thermodynamic data used in the calculations carried out in this study have been uploaded in a web page that can be accessed using the link <http://cesmec.fiu.edu/data/thermodata01.txt>. Except for Ca-perovskite (CaPv), the end-member thermodynamic properties are taken from the updated and internally consistent data base

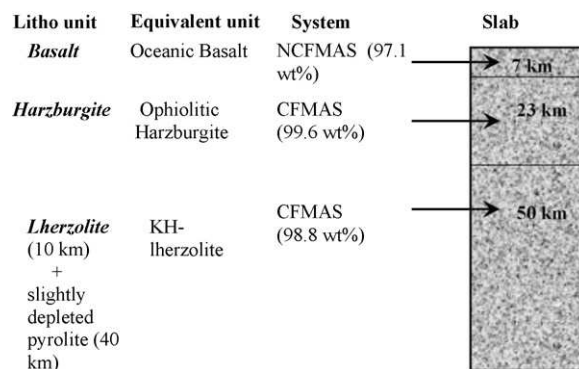


Fig. 1. Schematic representation of the different lithologic units that are assumed to constitute an approximately 80 km thick oceanic slab. The acronyms connected to the units indicate chemical systems that are used to represent the bulk compositions. The numbers beside the acronyms indicate the wt% that these systems constitute of the total chemical systems in the different units. N: Na₂O; C: CaO; F: FeO; M: MgO; A: Al₂O₃; S: SiO₂.

Table 1

Compositions of lithologic units in wt%. Additional components are neglected.

| | Average mantle | Normalized CFMAS | Ophiolitic Harzb | Normalized CFMAS | KH-Iherzol | Normalized CMAS | Average basalt | Normalized NCFMAS |
|--------------------------------|----------------|------------------|------------------|------------------|------------|-----------------|----------------|-------------------|
| SiO ₂ | 45.96 | 45.44 | 42.30 | 42.47 | 44.48 | 45.01 | 48.40 | 49.29 |
| Al ₂ O ₃ | 4.16 | 4.20 | 0.50 | 0.50 | 3.59 | 3.63 | 15.30 | 15.58 |
| FeO | 8.07 | 8.15 | 7.10 | 7.13 | 8.10 | 8.20 | 9.50 | 9.67 |
| MgO | 38.26 | 38.67 | 49.60 | 49.80 | 39.22 | 39.68 | 11.40 | 11.61 |
| CaO | 3.50 | 3.53 | 0.10 | 0.10 | 3.44 | 3.48 | 11.50 | 11.71 |
| Na ₂ O | | | | | | | 2.10 | 2.14 |
| Total | 98.95 | 100.00 | 99.60 | 100.00 | 98.83 | 100.00 | 98.20 | 100.00 |

CFMAS: CaO–FeO–MgO–Al₂O₃–SiO₂; NCFMAS: Na₂O–CFMAS; Harzb: harzburgite; Iherzol: Lherzolite.

of Fabrichnaya et al. (2004) that are well suited to high P–T calculations. The thermodynamic data have been derived by global optimization of a large number of experimental data on phase equilibria along with the available thermochemical and thermo-physical properties. The success of this optimized data base in reproducing experimentally determined phase relations have been demonstrated by Fabrichnaya (1998, 1999).

The CaPv properties are retrieved from the experimentally determined phase relations in the system CaO–MgO–SiO₂ (Akaogi et al., 2004), assuming that it has the same C_p vs. T relation as wollastonite (Fabrichnaya et al., 2004). The retrieved CaPv properties are internally consistent with the data of other end-member phases in Fabrichnaya et al. (2004) that have been used in this study. Kojitani et al. (2001) estimated the enthalpy of formation from oxides, $\Delta H_{f,o}$, of CaPv from extrapolation of heat of solution data for the compositional range $X(\text{CaSiO}_3) = 0\text{--}0.30$ in the CaSiO₃–CaGeO₃ binary join. From these data, we obtain heat of formation from elements, $\Delta H_{f,e}(1 \text{ bar}, 298 \text{ K}) = -1530.17 (\pm 8.82) (\pm 2\sigma)$, kJ/mol, as compared to our optimized datum of -1551.60 kJ/mol.

Stixrude et al. (2007) have recently calculated the stability field of CaSiO₃ perovskite at high pressure using density functional theory and predicted that cubic perovskite should transform to a tetragonal form at high pressure, and that the phase transition should have a positive P–T slope. The calorimetric data of Kojitani et al. (2001) and phase relations of Akaogi et al. (2004), from which we retrieved the thermodynamic properties of CaSiO₃ perovskite, pertain to perovskite of cubic symmetry. However, part of the P–T conditions within a slab, as discussed later, fall within the proposed field of stability of the tetragonal polymorph. Our density calculations for the slab P–T conditions are, however, based on the properties of cubic Ca-perovskite. If indeed the stable phase at these conditions is the denser tetragonal form, then the densities of the slab components would be somewhat higher than what we calculate, and thus support the qualitative conclusions that we finally arrive at about the penetration of the slab into the lower mantle.

The thermodynamic mixing properties of various components in different phases are taken from several sources, and approximated when direct data are lacking. The sources of data are: Ganguly and Saxena (1987), Saxena et al. (1993) and Wood (1979) for pyroxenes; Elkins and Grove (1990) for plagioclase feldspar, Ganguly et al. (1996) for aluminosilicate garnets, and Fabrichnaya et al. (2004) for the rest of the phases, except for majoritic garnet solid solution.

The mixing property of majoritic garnet is treated in terms of four end-member components, namely, pyrope, almandine, grossular and Mg-majorite, $^{\text{VIII}}(\text{Mg})_3^{\text{VI}}(\text{Mg}_{0.5}\text{Si}_{0.5})_2^{\text{IV}}(\text{Si})_3\text{O}_{12}$. Vinograd et al. (2006) have deduced the mixing property of pyrope and Mg-majorite components from static energy calculations. From their data, we find that the enthalpy of mixing in this join can be approximated in terms of a symmetrical solution model, $\Delta H^{\text{mix}} = A_0(H)X_{\text{Pyr}}X_{\text{Mg-maj}}$, for the compositional range of interest in the mantle mineralogy, with $A_0(H) = 5\text{--}9$ kJ/mol on 4-oxygen basis per formula unit. These values are compatible with the calorimet-

ric data of Saikia et al. (2007) if one ignores one datum at the pyrope-rich end. The entropy of mixing between Mg-majorite and Pyrope is assumed to be ideal. The Grs–Fe-majorite and Grs–Mg-majorite interactions are assumed to be the same as Grs–Alm and Grs–Prp interactions, respectively, in the ordinary aluminosilicate garnets. The remaining interactions in the garnet solid solution, which are among the aluminosilicate components, are assumed to be the same as in the aluminosilicate garnet solid solution model of Ganguly et al. (1996). Our entropy of mixing calculation implicitly assumes that there are no significant octahedral cations in majoritic garnet other than Mg and Al. A small amount of Fe²⁺ cation is also likely to be present in the octahedral sites, thereby slightly raising the entropy of mixing. There are, however, no data on site occupancies that are needed to account for this effect. To test the sensitivity of the results of our calculations to the mixing property of majorite garnet, we varied $A_0(H)$ between 0 and 9 kJ/mol for the majorite-pyrope binary join, and found no significant effect on the density value or garnet composition.

When adequate data are lacking for the mixing of a ferrous end-member component in a phase, it is taken to be the same as that of the corresponding Mg end member, as Fe and Mg typically mix with only a small positive deviation from ideality in rock forming minerals (Ganguly and Saxena, 1987). The Fe²⁺–Mg interaction is assumed to be ideal when the required data are not available. For the lack of thermodynamic data on the Mg- and Al-perovskite components with CaPv structure, we have treated the Ca-rich perovskite phase as a stoichiometric compound. However, according to the data of Litasov et al. (2005), a small amount of the above components (5–6 mol% Mg and 2–3 mol% Al) substitute in CaPv.

All solid solutions are treated in terms of the two parameter Guggenheim polynomial (also known as Redlich–Kister polynomial) representation of excess Gibbs free energy of mixing, ΔG^{XS} (e.g. Ganguly and Saxena, 1987), except for the aluminous perovskite, for which we used the mixing property data of Fabrichnaya (personal communication) that are formulated in terms of the compound energy or sublattice model (Hillert, 1998).

For the NCFMAS system used for oceanic basalt, we assumed that Na substitutes only in plagioclase and clinopyroxene, which are by far the major carriers of these components among the potential phases in a basalt composition. The jadeite component in clinopyroxene is assumed to mix ideally as we lack adequate data on the mixing properties between the jadeite and other components in clinopyroxene. However, the experimental data on the mixing property in binary jadeite–diopside join (Holland, 1980) may be closely approximated by a pseudo-ideal mixing behavior of the macroscopic components NaAlSi₂O₆ (jadeite: Jd) and CaMgSi₂O₆ (diopside: Di) (Ganguly and Saxena, 1987). Thus, it is very unlikely that the assumption of ideal mixing of the Jd component in clinopyroxene has any significant effect on the calculation of density of basaltic bulk composition as a function of pressure and temperature, especially considering that there is only 2.2 wt% Na₂O in the system. A small amount of Na would be incorporated in garnet at high pressure (Gasparik, 2000; Bobrov

and Litvin, 2008). The problem of partitioning of Na between garnet and clinopyroxene cannot be addressed at the present stage for the lack of adequate thermodynamic data. However, transferring a small amount of Na from high-pressure clinopyroxene to garnet is most unlikely to have any significant effect on the density structure of the basaltic component of a slab.

The different binary joins in a multicomponent solid solution have been combined according to the “shortest distance” method. In this method, the ΔG^{XS} of a multicomponent solution represents the sum of those at the bounding binaries, the compositions of which are obtained by normal projections from the composition in the multicomponent space. As discussed by Cheng and Ganguly (1994), this is, in general, a better method of estimating properties of multicomponent solution from those of the bounding binary joins, if one wishes to avoid the complications of ternary and higher order interactions. Overall, our calculations have been carried out with more detailed consideration of thermodynamic mixing properties of different phases than what seems to have been attempted so far in the computations of mantle mineralogy.

In thermodynamics, the equilibrium state of a system at a fixed P–T condition is given by the state of lowest Gibbs free energy, G . Thus, in each bulk composition, the equilibrium composition and modal abundance of minerals are calculated simultaneously by minimizing $G_{P,T}$ of the system, subject to bulk compositional constraints. The thermodynamic basis and numerical logic of the algorithm have been discussed in a series of pioneering papers by Eriksson and co-workers (e.g. Eriksson and Rosén, 1973; Eriksson, 1975), and the algorithm itself has been used in numerous computations in the fields of materials sciences and chemical engineering, and also in several earlier studies in the Earth and planetary sciences, such as Saxena and Eriksson (1983), Saxena and Eriksson (1986) and Saxena (1996).

The bulk density of a stable mineral assemblage is calculated from their modal abundances and equations of state (EoS) data for the end-members (Saxena et al., 1993; Fabrichnaya et al., 2004), assuming that the density of a mineral solid solution is given by a linear combination of the end-member densities (ideal volumetric behavior). The P–V relations have been treated with the second order Birch–Murnaghan EoS formulation (Birch, 1952). Further details about the formulations of P–T dependence of volumetric properties can be found in Saxena et al. (1993) and Fabrichnaya et al. (2004). The mineral phases included in the G minimization scheme are Mg–Fe olivine (Ol), Mg–Fe–Al–Ca orthopyroxene (Opx), Mg–Fe–Ca–Al high- and low-pressure clinopyroxenes (HpCpx and LpCpx), plagioclase (Plag), Mg–Fe–Ca garnet/majorite (Grt, Mj-Grt), Mg–Fe spinel (Spln), Mg–Fe wadsleyite (Wads), Mg–Fe ringwoodite (Rng), Mg–Fe–Al ilmenite or akimotoite (Ilm), Mg–Fe–Al perovskite (MgPv), Ca-perovskite (CaPv), magnesiowüstite (Mg–Wu), stishovite (Stv) and all rock-forming pure minerals in the CaO–MgO–FeO–Al₂O₃–SiO₂ system.

2.2. Adiabatic density structure of the mantle

To test the validity of the density data obtained from free energy minimization calculations, we first calculate the adiabatic density profile of the mantle within the depth interval of 200–800 km and compare the data with the densities given in the Preliminary Reference Earth Model or PREM (Dziewonski and Anderson, 1981) and also with the density profile calculated by Litasov et al. (2005) from their high P–T experimental phase equilibrium data for pyrolite bulk composition (Fig. 2). The latter workers calculated the densities along a mantle adiabat using available thermo-physical properties of mantle minerals and the third-order Birch–Murnaghan equation of state (Birch, 1952).

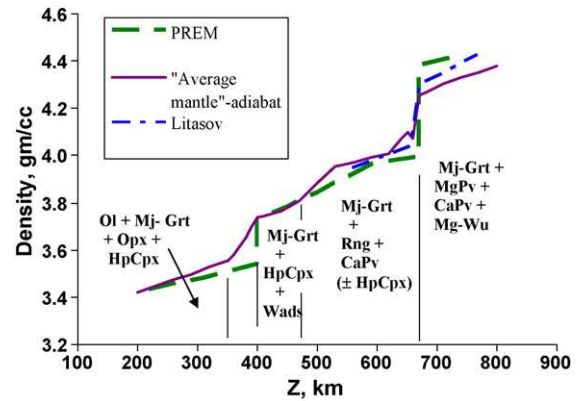


Fig. 2. Calculated density vs. depth in the Earth's mantle along an adiabatic (isentropic) P–T profile and comparison with the data in PREM (Dziewonski and Anderson, 1981) and the experimental data of pyrolite along a mantle adiabat (Litasov et al., 2005). Some of the critical minerals with major influence on the density jumps are indicated within the different fields. Ol: olivine, Mj-Grt: majoritic Garnet, HpCpx: high-pressure clino-pyroxene, Opx: orthopyroxene, Wads: wadsleyite (β -Mg₂SiO₄), Rng: Ringwoodite (γ -Mg₂SiO₄), MgPv: Mg-perovskite, CaPv: Ca-perovskite, Mg–Wu: magnesiowüstite.

On the basis of the thermo-chemical and -physical parameters from Saxena et al. (1993) for mantle minerals, we calculate an adiabatic gradient of 0.64 °C/km for an upper mantle composed of 60 vol% olivine, 20 vol% orthopyroxene, 10 vol% garnet and 10 vol% clinopyroxene, using the well known relation $(\partial T/\partial Z)_S = \alpha g/C_p$, where S stands for the entropy, α for the coefficient of thermal expansion, g for the acceleration due to gravity, and C_p for the specific heat capacity at constant pressure. For both α and C_p of an assemblage, we used the weighted average values of the constituent minerals. A change of ~5% of the modal abundance of the minerals does not have any significant effect on the adiabatic temperature gradient. Calculation of the density profile at 1300 °C shows very good agreement with the PREM density at 200 km depth. Thus, we assume that at this depth, the average mantle temperature is 1300 °C, and thereby construct an adiabatic profile down to 800 km depth. This exercise yields 1594 °C at 660 km depth. Where there are major phase transitions such as at 400 and 660 km depths, the adiabatic (isentropic) thermal profile must have sharp temperature changes to compensate for the change of entropy due to phase transitions so that the net entropy is conserved (Saxena, 1996). However, these temperature changes (~40 °C) are not large enough to cause significant density changes.

Overall, our calculated adiabatic density profile of the mantle is in good agreement with the PREM density profile. The main differences between our calculated and PREM data are (a) the degree of sharpness of the density jump at 400 km depth, (b) a small density jump in our calculations at 500 km depth, while such a jump is absent in PREM, and (c) the magnitude of the density jump at 660 km depth. However, our results for the degree of sharpness of the 400 km discontinuity and magnitude for the 660 km discontinuity are permissible by seismic data (Lawrence and Shearer, 2006). At 500 km depth, PREM does not show any effect of the phase transformation between the Mg₂SiO₄ polymorphs, wadsleyite (Wads) and Rng. The phase transformation must be global, but it is not detected seismically everywhere, likely due to limitations in the resolution of the seismic techniques used to develop the PREM model (e.g., Lawrence and Shearer, 2006).

Our calculated density data are in good agreement with the adiabatic pyrolite (Ringwood, 1982) densities determined by Litasov et al. (2005) around the 660 km discontinuity. Their data also show a smaller density jump at 660 km depth than that in the PREM. The larger density jump in PREM relative to that found in this study

and by Litasov et al. (2005) for a homogeneous mantle model may be partly due to compositional difference between the upper and lower mantles, a concept that has been discussed repeatedly in the literature (e.g. Christensen and Yuen, 1984; Griffiths and Turner, 1998). The flattening of the density profile between 600 and 660 km shown in PREM is in contrast to the adiabatic density profiles calculated in this study and by Litasov et al. (2005).

The degree of overall agreement of our calculated adiabatic mantle density profile with PREM and that of Litasov et al. (2005) suggests that our computational approach yields reliable density data in the CFMAS system at the P–T conditions of the Earth’s upper mantle and the transition zone. The relative densities of the different lithological units should be even better since all density calculations are based on the same thermodynamic data base and computational procedure. The molar abundances of the phases along the mantle adiabat are shown in Fig. 3. Our calculations do not show the presence of ilmenite (akimotoite) along an average mantle adiabat. This rather surprising result is, however, in agreement with the calculations of the adiabatic mantle mineralogy, based on a pyrolite model, by Ricard et al. (2005).

3. Thermal structures of slabs

We calculate thermal structure within and around a downgoing slab (Fig. 3) using a finite difference algorithm (McKenzie, 1969; Toksöz et al., 1973) that has been widely used in slab thermal modeling studies (e.g., Stein and Stein, 1992; Kirby et al., 1996; Bina and Navrotsky, 2000). Calculation of slab thermal structures lead to a range of geotherms depending on the various assumptions employed. Here our objective is not to provide a definitive thermal profile for any particular slab, but to explore a general range

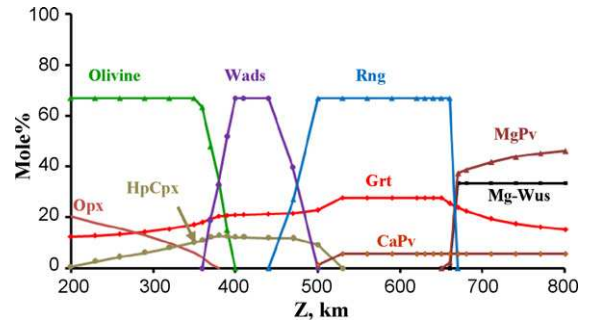


Fig. 3. Molar percentage of minerals as a function of depth along the mantle adiabat (Fig. 8) for the average mantle bulk composition, as calculated in this work. The symbols indicate the P–Z conditions of calculations.

of plausible geotherms that develop due to variation of subduction parameters and ages characterizing the coldest (older, faster) to the warmest (younger, slower) slabs.

Before an oceanic lithosphere reaches the trench, its thermal structure is defined using the GDH1 thermal plate model (Stein and Stein, 1992), which reaches steady state at an age of ~70 Myr. We assume the material properties to be independent of P–T condition within the range typically used in thermal modeling studies ($C_p = 1.17$ kJ/kg K; K (thermal conductivity) = 3.14 W/m K; $\alpha = 3.1 \times 10^{-5} K^{-1}$), a lithospheric thickness of 95 km and a basal temperature of 1450 °C (e.g., Kirby et al., 1996). Isotherms within the slab are advected downward during subduction, heated by conduction from a hotter mantle, reaching a maximum depth proportional to the product of the vertical descent rate and age. Known as the thermal parameter (TP) (e.g., Weins and Gilbert, 1996), this

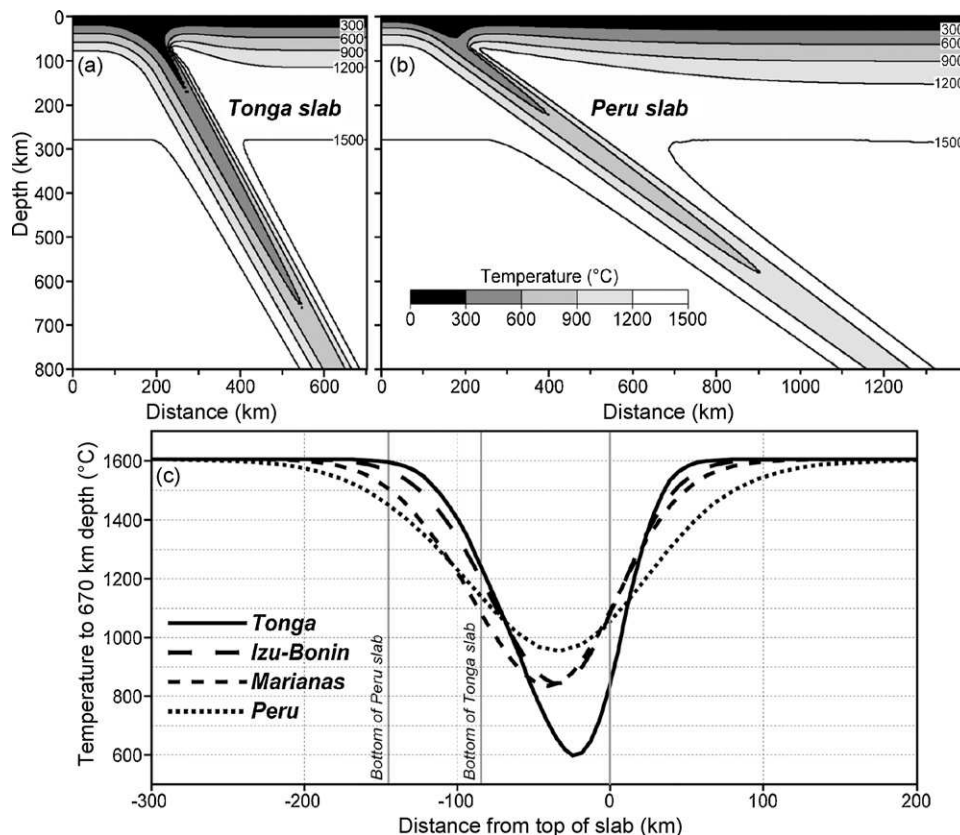


Fig. 4. Calculated thermal profiles of the (a) Tonga- and (b) Peru-type slab-mantle systems as function of depth, and (c) thermal profiles at 670 km depth of four different slabs with wide range of ages at the trench (41–155 Myr), vertical descent rate (4.4–10.7 cm/yr) and average subduction angles (35–64°). Note that the thermal profiles of the Tonga- (110 Myr) and Peru-type (41 Myr) slabs represent the extreme limits.

product is a convenient parameter for comparing the temperatures of various slabs as function of depth.

To understand the effect of slab age and other subduction parameters, we calculate the thermal structures of four slabs and the surrounding mantle environments. The chosen slabs along with their parenthetical properties (Weins and Gilbert, 1996) indicating age at the trench, vertical descent rate, V_z , average subduction angle, θ , and TP are (a) Tonga (110 Myr, $V_z = 15.5$ cm/yr, $\theta = 53^\circ$, TP = 17,050 km); (b) Marianas (155 Myr, $V_z = 5.9$ cm/yr, $\theta = 64^\circ$, TP = 9145 km); (c) Izu-Bonin (145 Myr, $V_z = 4.7$ cm/yr, $\theta = 51^\circ$, TP = 6815 km) and (d) Peru (41 Myr, $V_z = 4.4$ cm/yr, $\theta = 35^\circ$, TP = 1800 km). For Tonga, we use a higher value of TP (Kirby et al., 1996) so that its calculated thermal structure represents a cold end-member model.

We find that the computed thermal structures of Tonga and Peru (Fig. 4), which have the largest and smallest values of TP, respectively, represent end-member thermal conditions among the chosen set of slabs that encompass a wide range of age and subduction parameters, with Tonga being the coldest and Peru being the warmest. Our thermal profile of the Tonga slab (Fig. 4a) is virtually identical to that published by Kirby et al. (1996), who used the same numerical code and identical model parameters as used in our work. Fig. 4c shows the temperature profiles of Tonga, Izu-Bonin, Marianas and Peru as function of horizontal distance from the top of each slab at the 670 km depth, which is roughly the depth of seismic discontinuity defining the top of the lower mantle.

We choose the thermal structures of Tonga and Peru to evaluate the effect of large variation of age and subduction parameters on the density structures of the slab–mantle systems. It should be noted that the illustrations in Fig. 4 are simplified first-order representations of the thermal structures of the specific slabs, since there are changes of slab geometries with depth, and additional complications resulting from variations of physical properties, mantle convection, feedback of the enthalpy change of mineral reactions etc. that could influence the details of the thermal structures. These calculations are meant to illustrate approximate limiting thermal models for slabs with large variation of age at the trench, vertical velocity and average subduction angle. Thus, instead of saying thermal structures of Tonga and Peru slabs, we would henceforth refer to the calculated thermal structures as those of Tonga-type (old) and Peru-type (young) slabs.

4. Density profiles of slabs within and around the transition zone

We first combine the results of the calculation of densities of different lithologic units as function of P and T with the thermal structures of the Tonga- and Peru-type slabs to develop the density profiles of the slab–mantle systems at selected depths within and around the transition zone (400–670 km depth). Based on the density and thermal profiles illustrated in Figs. 2 and 4, we choose 370 km (12.6 GPa), 500 km (17.4 GPa) and 670 km (23.8 GPa) to evaluate the effects of phase transformations on the density contrast between a slab and the surrounding mantle. For the first two depths, transformations to denser assemblage take place within the slabs, but not in the ambient mantle, whereas the reverse is true for the 670 km depth. In addition, we select 640 km (22.6 GPa) and 700 km (25.1 GPa) depths to evaluate the effects of downward deflection of thermal profiles within a slab (Fig. 4) on its density profile. The relationship between pressure and depth is obtained from the PREM (Dziewonski and Anderson, 1981).

The composite density (ρ) profiles at 370 and 670 km, which represent depths near the top and bottom of the transition zone, are illustrated in Fig. 5 for the Tonga- and Peru-type slabs. In this figure and elsewhere we use the terms basalt, harzburgite and lherzolite

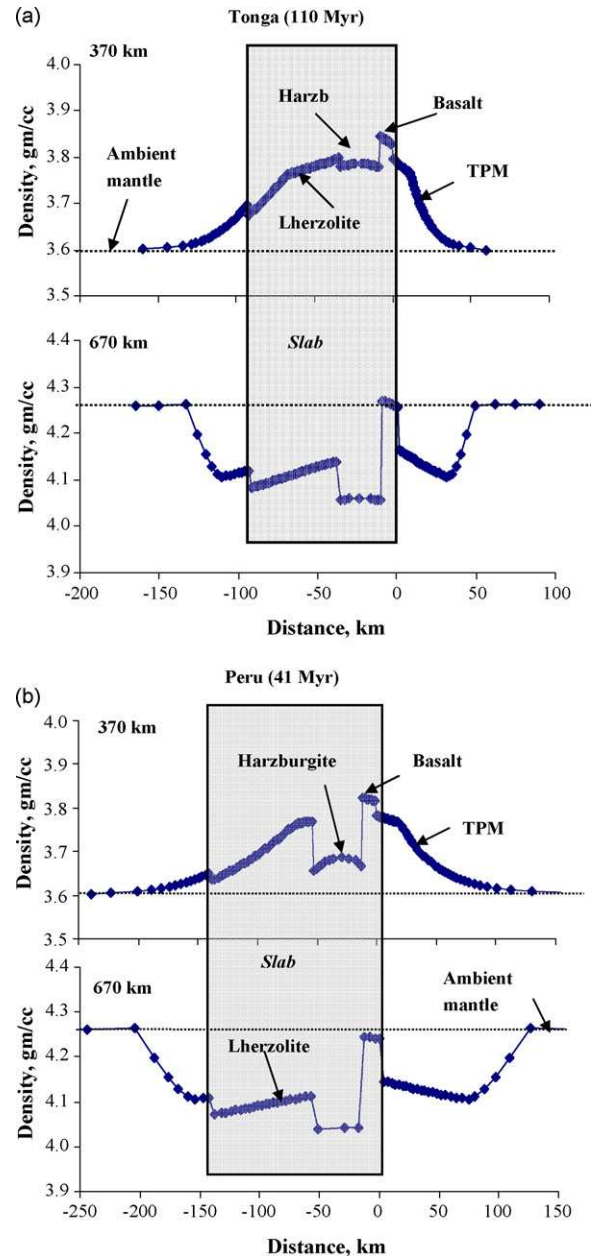


Fig. 5. Calculated equilibrium density profiles in two lithologically stratified slabs, (a) Tonga-type (110 Myr at the trench) and (b) Peru-type (41 Myr at the trench), and the surrounding mantle at the 370 km and 670 km depths as function of distance from the top of the slabs. TPM: thermally perturbed mantle layer near a slab (see Fig. 3).

to denote specific bulk compositions, and not the rock types, and TPM to denote the thermally perturbed mantle near a slab (Fig. 4). Despite large difference for the age at the trench, subduction angle, and vertical descent velocity, the density profiles of the two slabs are quite similar, except that at the 370 km depth, the harzburgite layer in the young Peru-type slab is significantly lighter than that in the Tonga-type slab. This difference between the density of harzburgite in the two types of slabs is mainly due to the progressive decrease of wadsleyite to olivine ratio from ~99 to 1 as the temperature increases from 600 to 950 °C, which correspond approximately to the temperature minimum in the Tonga-type and Peru-type slabs, respectively (Fig. 4).

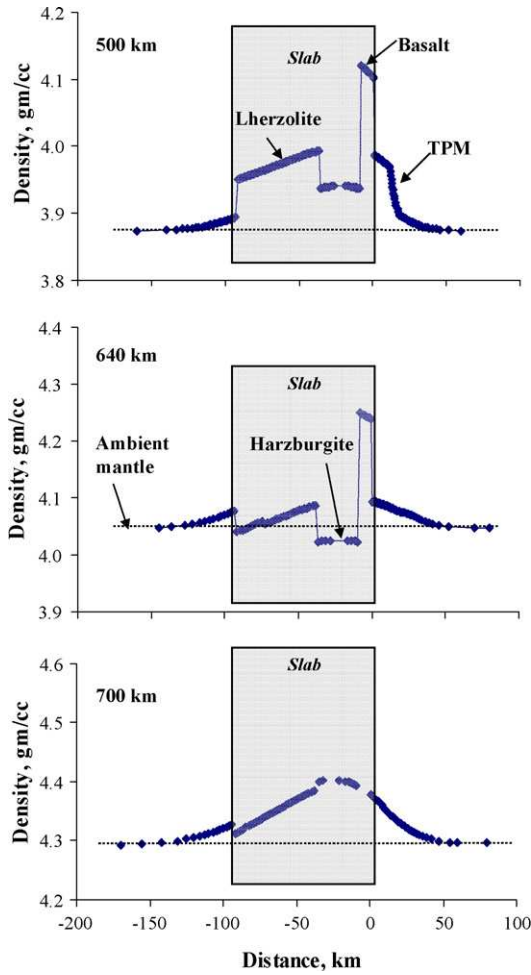


Fig. 6. Calculated equilibrium density profiles of Tonga-type (110 Myr at the trench) slab and surrounding mantle at 500, 640 and 700 km depths.

Fig. 6 shows the density profiles of the Tonga-type slab at 500, 640 and 700 km depths. The density profiles in the Peru-type slab at these depths are similar, despite a difference of $\sim 300^\circ\text{C}$ between the thermal minima within the two slabs. This is because of weak temperature effect on the density of mantle minerals at high pressures (Saxena et al., 1993). Temperature difference between the slabs causes significant difference in the density structure only when it leads to a difference in the phase assemblages, such as at the 370 km depth for the Tonga- and Peru-type slabs (Fig. 5a and b).

The basalt layer of the slab is omitted at 700 km depth since relatively Al-rich Mg-perovskite and additional new high-pressure phases appear in basalt at ~ 720 km depth (Hirose et al., 1999) for which we do not have adequate thermodynamic data for free energy minimization calculations. It should be noted that the thermally perturbed mantle adjacent to a slab is heavier than the ambient mantle at all depths, except at 670 km. Similar to the slabs, the TPM at the 670 km is lighter than the ambient mantle. The lower density of a slab and TPM at this depth is due to negative P–T slopes of perovskite forming reactions.

We illustrate in Fig. 7 the molar percentages of phases as function of depths along thermal profiles approximately at the centers of the different lithologic units within the Tonga-type slab. These thermal profiles, along with the mantle adiabat, are illustrated in Fig. 8. The sequence of appearance and coexistences of olivine, wadsleyite and ringwoodite may be understood by comparing the thermal profiles with the P–T stability diagram of these phases in

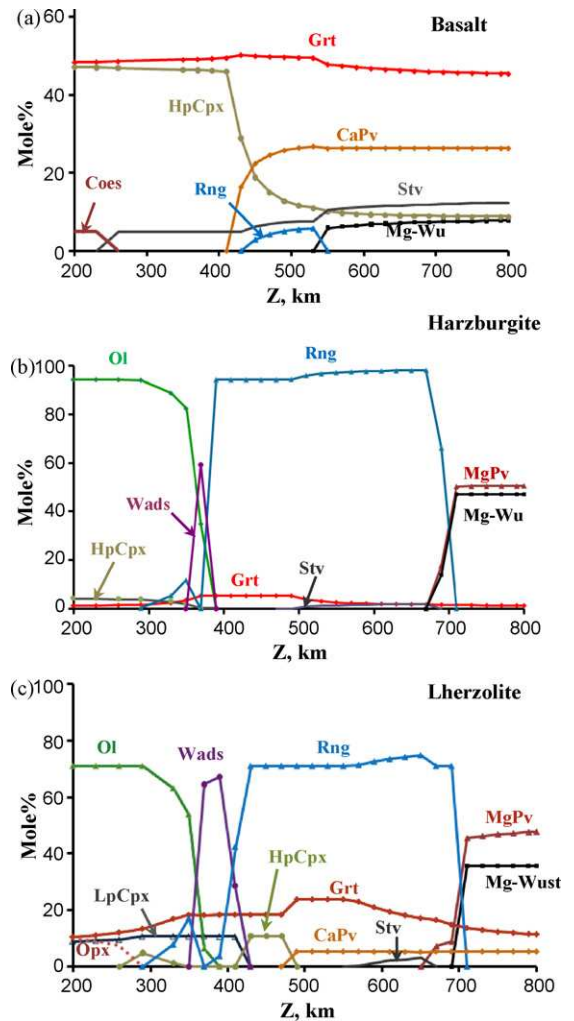


Fig. 7. Molar percentage of minerals in (a) basalt, (b) harzburgite and (c) lherzolite bulk compositions along three thermal profiles within the Tonga-type slab that are approximately half-way into the respective lithologic units, as illustrated in Fig. 8. The symbols indicate the P–Z conditions of calculations. LpCpx: low pressure clinopyroxene, Stv: Stishovite. Other abbreviations: as in Fig. 2.

the $\text{Fe}_2\text{SiO}_4\text{--Mg}_2\text{SiO}_4$ system (Vacher et al., 1998; Gasparik, 2003). Fig. 9 shows the density profiles of the different components of the Tonga-type slab and ambient mantle as function of depth.

It is obvious that in the above discussion of density and phase assemblage evolution, we have treated both cold and young slabs

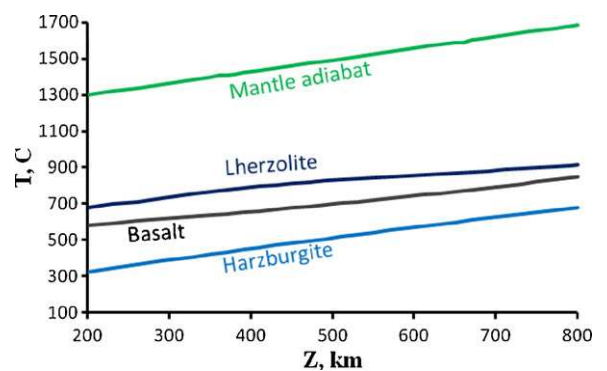


Fig. 8. Average adiabatic thermal profile of the Earth's mantle and thermal profiles nearly at the centers of different lithologic units of the Tonga-type slab.

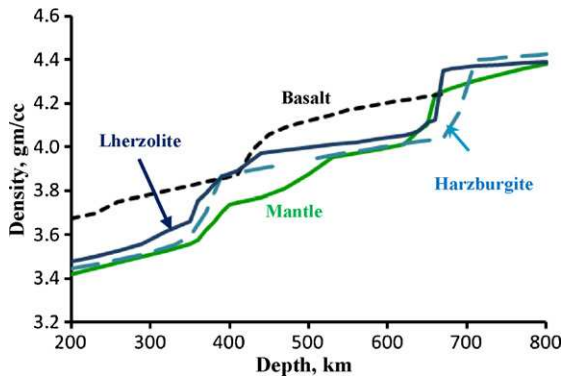


Fig. 9. Comparison of the density profile of the ambient mantle with those of the different lithologic components of the Tonga-type slab along the thermal profiles illustrated in Fig. 8.

as completely anhydrous. However, as pointed out by Bose and Ganguly (1995), and subsequently re-iterated by other workers (e.g. Bose and Navrotsky, 1998; Komabayashi and Omori, 2006), dense hydrous magnesium silicates (DHMS) would form from serpentine at the top part of a Tonga-type cold slab. These DHMS phases may make a cold slab somewhat heavier than what we calculate.

5. Penetration of the slabs into the lower mantle

5.1. The depth to neutral buoyancy

Fig. 10 shows the density of ambient mantle, mean densities of the Tonga (old)- and Peru (young)-type slabs and their least dense and most dense lithological components, namely harzburgite and basalt, respectively, as function of depth between 370 and 730 km, assuming attainment of thermodynamic equilibrium. The

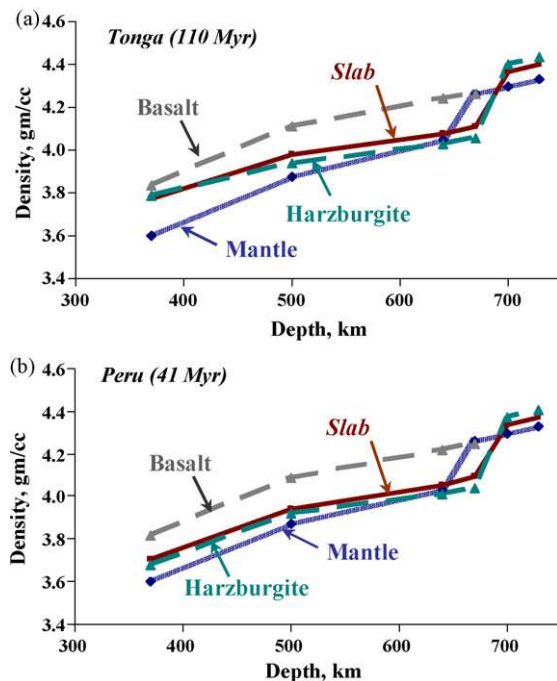


Fig. 10. Mean equilibrium density vs. depth of (a) Tonga (old)- and (b) Peru (young)-type slabs, surrounding ambient mantle, and the most dense (basalt) and least dense (harzburgite) slab components. The mean densities have been calculated at specific depths that are shown by symbols so that the density variations between two successive steps have been smoothed out.

mean density of basalt at ~ 700 km depth must be higher than that obtained by the projection of the ρ vs. Z trend because of the appearance of new denser phases (Hirose et al., 1999, 2005), which have not been included in our calculations, as discussed above. The mean densities of the different slab components and of the slab as a whole are calculated at six different depths that are indicated by symbols. As should be evident from the detailed calculation of density profiles of different components of the Tonga slab (Fig. 9) along selected thermal profiles, the density jumps between 370 and 500 km have been smoothed out in the calculations shown in Fig. 10. In other words, the density profiles of different units within 370 and 500 km depths represent roughly their respective average profiles.

Since a slab is denser than the ambient mantle at all depths down to 660 km, the negative buoyancy force would tend to cause sinking of the slab into the lower mantle unless it is resisted by such factors as viscosity jump at 660 km depth, metastable persistence of olivine (Tetzlaff and Schmelting, 2000) and the dynamics of slab roll back. Bina (1996) has calculated the local buoyancy of a subducting slab as a function of depth due to thermal deflection and polymorphic transition of olivine \rightarrow Wads \rightarrow Rng, and its contributions to stresses in subducting lithosphere. We, however, calculate the net buoyancy of the entire slab. We first calculate the depth to which a slab would need to penetrate into the lower mantle to achieve neutral buoyancy, if the formation of higher density assemblage in the slab is inhibited by kinetic factors and the different components of the slab are mechanically coupled. We then consider the experimental data on reaction kinetics to evaluate if the slabs could actually achieve a state of neutral buoyancy within the lower mantle or would continue to sink once it breaks through the 660 km discontinuity.

The depth to neutral buoyancy of a slab is obtained by equating the total weight of the slab with that of the displaced upper and lower mantle materials. Assuming that a slab behaves as a mechanically coherent unit, we derive

$$Z_{1s} = -\frac{Z_{us}(\Delta\bar{\rho}_u)}{\Delta\bar{\rho}_l} \quad (1)$$

where Z_{1s} is the vertical distance (positive downwards) that a slab penetrates into the lower mantle, Z_{us} is the vertical length of the slab in the upper mantle, and $\Delta\bar{\rho}$ is the difference between the mean densities of the slab and the adjacent ambient mantle in the upper (u) and lower (l) zones. Z_{us} is taken to be 580 km, which is the depth of the lower mantle (660 km) minus the thickness of the slab (80 km).

The quantity $\Delta\bar{\rho}_u$ is given by $\sum(\Delta\rho_i\Delta Z_i)/580$, where ΔZ_i is a discrete vertical length segment of a slab and $\Delta\bar{\rho}_i$ is the mean density difference between the slab segment and the ambient mantle. This procedure yields $\Delta\bar{\rho}_u$ (Peru) = 0.036 and $\Delta\bar{\rho}_u$ (Tonga) = 0.041 gm/cm³, assuming that the effects of thermal deflection and compositional difference up to the 370 km depth causes a density difference between a slab and the surrounding mantle of 0.03 gm/cm³. This assumption is based on the results of our calculation on the density difference between a slab and surrounding mantle at the 640 km depth, where there is no phase transformation in any lithologic unit. The quantity in the denominator of Eq. (1) is assumed to be given by the density of a slab minus that of the lower mantle at 670 km depth (Fig. 10). Densities of a slab and the lower mantle change as function of depth. However, as long as there is no phase transformation in the subducting slab and the lower mantle below 670 km depth, the densities should change quite similarly in response to increasing P–T condition so that $\Delta\bar{\rho}_l$ should remain approximately constant, at least until the depth to neutral buoyancy. With these data and assumptions, we obtain Z_{1s} (Peru: young) ~ 100 km and Z_{1s} (Tonga: old) ~ 125 km.

Mosenfelder et al. (2001) have addressed the problem of metastable survival of olivine within slabs of different vertical descent velocities and ages on the basis of the thermal structures of slabs and experimental data on the kinetics of transformation of olivine to wadsleyite and ringwoodite. From their analysis, we find that there is essentially no kinetic hindrance to the polymorphic transformation of Mg_2SiO_4 in the young Peru-type slabs. However, olivine would persist metastably around the thermal minimum of an old Tonga-type slab down to ~ 600 km depth. Seismic data also suggest survival of a metastable olivine wedge (MOW) up to 550–630 km within old subducting slabs such as those associated with the Pacific plate (Jiang et al., 2008), at Izu-Bonin (Iidaka and Suestuga, 1992) and at Mariana (Kaneshima et al., 2007). Thus, the depth to neutral buoyancy of the Tong-type slabs has been overestimated in the calculation presented above. Readjustment of the density difference between the slab and mantle to account for a MOW yields a depth to neutral buoyancy of ~ 105 km within the lower mantle. The readjustment of density was carried out by progressively reducing the density of the slab between 370 and 600 km depth, using the data of Mosenfelder et al. (2001) on the volumetric proportion of olivine that survives metastably as function of depth in a Tonga-type old slab. Here we have ignored the fact that olivine within a slab is somewhat denser than that in the ambient mantle at the same depth owing to the effect of thermal deflection. Thus, the depth to neutral buoyancy within the lower mantle could be somewhat greater than 105 km for the old Tonga-type slabs. In summary, we conclude that essentially all slabs would attain neutral buoyancy after they penetrate ~ 100 km into the lower mantle if the formation of perovskite bearing assemblage in the slabs is kinetically inhibited until the time of attainment of neutral buoyancy. (Note that the effect of greater thermal deflection on the density of a Tonga-type cold slab relative to that of a Peru-type young slab is largely offset by the presence of a MOW.) In the following discussion, this kinetically controlled depth to neutral buoyancy will be referred to simply as “depth to neutral buoyancy” or “DNB”.

Kubo et al. (2002) have studied the kinetics of post-spinel transformation in Mg_2SiO_4 at high P–T conditions. Their data have not been presented in a form that permits calculation of the extent of post-spinel transformation as a function of the depth of penetration of a slab into the lower mantle. However, Kubo et al. (2002) illustrated the relationship between time and temperature for 10% transformation at 1 (± 0.5) GPa and 4.5 (± 1) GPa over-pressure (ΔP) beyond the equilibrium boundary of the spinel = perovskite + periclase reaction, as determined by Irifune et al. (1998). From these data, one could infer whether or not complete post-spinel transformation is likely to be achieved within young and old slabs before these penetrate to the DNB.

The equilibrium P–T boundary for spinel to Mg-perovskite plus Mg–Wu transition has recently been revised by Fei et al. (2004). However, in order to be consistent with the presentation of kinetic data of Kubo et al. (2002), we determine the temperature and depth of the thermal minimum within a slab where a specific ΔP value is achieved by comparing the P–T trajectory of the thermal minimum with the P–T data of Irifune et al. (1998) for the spinel to Mg-perovskite plus Mg–Wu transition. Thus, we find that for a young Peru-type slab, the temperature at the thermal minimum for $\Delta P = 1$ GPa is $\sim 960^\circ\text{C}$ ($Z \sim 675$ km or 85 km above the DNB) and that for $\Delta P = 4.5$ GPa is $\sim 1000^\circ\text{C}$ ($Z \sim 755$ km or 5 km above the DNB). At these conditions, 10% post-spinel transformation is achieved at ~ 14 days and ~ 20 h, respectively. For an old Tonga-type slab, no significant post-spinel transformation could be achieved at $\Delta P = 1$ GPa, as noted by Kubo et al. (2002), but at $\Delta P = 4.5$ (± 1) GPa, the temperature is $\sim 655^\circ\text{C}$ and $Z \sim 780$ (± 20) km, which is, within errors, the same the DNB. At this condition, 10% transformation is achieved at

~ 15 yrs (that corresponds to the time taken by the slab to descend by ~ 2.3 m in vertical distance).

Although the data of Kubo et al. (2002) are not adequate for calculation of the time scale of $\sim 100\%$ post-spinel transformation, the above calculations suggest that complete transformation would certainly be achieved in young slabs, and very likely in the old slabs as well, much before they penetrate to the DNB. Consequently, the slabs would remain negatively buoyant and continue to subduct into the lower mantle. In other words, once a slab penetrates into the lower mantle, it seems destined to descend all the way to the core-mantle boundary. Indeed, Grand et al. (1997) and van der Hilst et al. (1991) show tomographic images that suggest sinking of some slabs to the base of the lower mantle. (The recently discovered post-perovskite transformation (Murakami et al., 2004; Oganov and Ono, 2004), which should take place in the mantle at ~ 2700 km depth, has positive P–T slope, and would thus enhance the buoyancy force for a slab’s descent.)

5.2. Coupling density profiles with scale model experiments

Using viscous fluid experiments scaled to mantle conditions, Kincaid and Olson (1987) carried out a variety of descending slab experiments to evaluate the combined effects of density variation, viscosity jump, ridge boundary condition (fixed vs. free) and trench migration. A minimum viscosity contrast of 10^3 between the slab and lower mantle was needed to maintain tabular shape during subduction. Kincaid and Olson (1987) found that the behavior of the slabs at the 660 km discontinuity could be related to a normalized slab density anomaly, R , which is given by

$$R = \frac{\rho_s - \rho_{lm}}{\Delta\rho_u} \quad (2)$$

In the scale model experiments, each unit (slab, upper layer and lower layer) had uniform properties. It was found that if $R > 0.5$, the slabs in the experimental system penetrate into the lower layer as fairly undeformed units, whereas if $R < -0.2$, slabs with dip angles of $40\text{--}48^\circ$ bend at the top of this layer when there is a viscosity jump of a factor of ~ 11 along with a fixed ridge boundary condition (that leads to trench migration or slab roll back), followed later by subduction at a slower rate. Partial direct penetration was observed with the same viscosity jump and R value for free ridge boundary condition and dip angle of $58\text{--}86^\circ$.

To use the results of the scale experiments, we use average density ($\bar{\rho}$) values for each unit in Eq. (2). Furthermore, we use the density of a slab at the 500 km depth as its mean density (which is roughly the mean slab density within the transition zone), since we have not carried out detailed calculations of the density structure of a slab at $Z < 370$ km depth. Taking into account the problem of metastable survival of olivine in cold slabs, this procedure, which obviously overestimates the value of R , yields $R < -7.0$. (Note that in the absence of perovskite forming transitions within a slab, the quantity in the numerator of Eq. (2) is negative.) Thus, provided that the scale model experiments adequately captured the dynamics of the slab–mantle systems, our calculations suggest that any slab with dip angle of $40\text{--}50^\circ$ would bend at the 660 km discontinuity, if there is a viscosity jump of at least by a factor of ~ 11 and trench migration. Note that smaller the dip angle, the easier it is for a slab to flatten at the 660 km depth.

The scale model experiments were not carried out at a sufficiently wide range of conditions to enable us to evaluate as to what extent the above conditions may be relaxed and still have deflection/flattening of a slab at the 660 km depth. A slab that is deflected at this depth would eventually sink into the lower mantle due to negative buoyancy force, especially after a period of thermal relaxation leading to transformations to per-

ovskite. Thus, as emphasized by Griffiths and Turner (1998), seismic tomographic images of patches of horizontal slabs at the 660 km discontinuity should not be interpreted to imply that those slabs would not eventually penetrate into the lower mantle.

6. The fate of basalt and harzburgite layers

As illustrated in Figs. 9 and 10, the top basalt layer of both old (Tonga-type) and young (Peru-type) slabs is denser than the ambient mantle and other components of the slab down to 660 km discontinuity. At the 660 km discontinuity, the basalt layer has approximately the same density as that of the lower mantle. Thus, unlike what has been advocated earlier (Anderson, 1989; Irifune and Ringwood, 1993), our calculations do not seem to suggest “peeling off” of the basalt layer by buoyancy force from the rest of a slab, leading to the formation of “perched eclogite” or “piclogite” layer within the transition zone. Under conditions that a slab penetrates directly into the lower mantle, the top basalt layer of the slab would also do so. The tendency of the basalt layer to sink into the lower mantle is further enhanced by the formation of Al-rich perovskite at ~720 km depth (Hirose et al., 1999) once the slab has reached this depth (additional transformations to denser phases in the MORB composition at greater depths have been reported by Hirose et al., 2005). Hoffmann and White (1982) envisioned separation of the basalt layer from the rest of the slab, and subsequent sinking to the base of the lower mantle. Our density data are compatible with this model. However, whether or not a denser basalt layer separates and sinks into the lower mantle as a separate unit would depend on the extent of mechanical coupling between the basalt and the underlying harzburgite layers.

Previous studies have shown that the thermal deflection of the olivine/wadsleyite and ringwoodite/perovskite equilibrium phase boundaries have a controlling influence on the state of stress in the slab, subduction rates, and the fate of slabs as they come in contact with the lower mantle (e.g., Bina, 1996; Bina et al., 2001). Such studies have generally not considered the influence of the phase evolution of the individual slab components. The present study suggests a significantly denser basalt layer, compared to the rest of the slab, and a relatively low density harzburgite layer. These density contrasts could have a profound influence on slab dynamics, especially as the lower mantle is approached. Does the significant density contrast between basalt and harzburgite layers (Figs. 9 and 10) cause the slab to grossly deform upon contact with the lower mantle? How would such deformation influence the state of stress throughout the entire slab and affect subduction rates? While these questions are beyond the scope of the present study, the results presented here provide new constraints on the phase and density structure of subducting slabs that should help future analyses to address these issues.

Acknowledgments

We are grateful to Dr. Gunnar Eriksson for his advice and logistic support in the thermodynamic computational aspects of this paper. Thanks are due to two anonymous reviewers for helpful comments and to Prof. Dave Rubie for his editorial handling of the paper. The senior author (JG) gratefully acknowledges the support from the NASA Cosmochemistry grant NNG04GG26G and would like to thank the Alexander von Humboldt foundation for support during the final stage of preparation of this manuscript in Germany. Thanks are also due to Carnegie-DOE alliance, Geophysical Laboratory, Washington, DC for support to CeSMEC.

References

- Akaogi, M., Yano, Y., Tejima, H., Kojitani, H., 2004. High-pressure transitions of diopside and wollastonite: phase equilibria and thermochemistry of $\text{CaMgSi}_2\text{O}_6$, CaSiO_3 and CaSi_2O_5 – CaTiSiO_5 system. *Phys. Earth Planet. Int.* 143–144, 145–156.
- Anderson, D.L., 1989. *Theory of the Earth*. Blackwell, Boston, 366 pp.
- Bina, C.R., 1996. Phase transition buoyancy contributions to stresses in subducting lithosphere. *Geophys. Res. Lett.* 23, 3563–3566.
- Bina, C.R., Stein, S., Marton, F., Van Ark, E.M., 2001. Implications of slab mineralogy for subduction dynamics. *Phys. Earth Planet. Int.* 172, 51–66.
- Bina, C.R., Navrotsky, A., 2000. Possible presence of high-pressure ice in cold subducting slabs. *Nature* 408, 844–847.
- Birch, F., 1952. Elasticity and the constitution of the Earth's interior. *J. Geophys. Res.* 57, 227–286.
- Bobrov, A.V., Litvin, Y.A., 2008. Experimental study of the $\text{Mg}_3\text{Al}_2\text{Si}_3\text{O}_{12}$ – $\text{Na}_2\text{MgSi}_5\text{O}_{12}$ system at 7.0 and 8.5 GPa: implication for the formation of Na-bearing garnets. *Doklady Earth Sci.* 419, 339–343.
- Bose, K., Ganguly, J., 1995. Experimental and theoretical studies of the stabilities of talc, antigorite and phase A at high pressures with applications to subduction processes. *Earth Planet. Sci. Lett.* 136, 109–121.
- Bose, K., Navrotsky, A., 1998. Thermochemistry and phase equilibria of hydrous phases in the system Mg – SiO_2 – H_2O : implications of volatile transport to the mantle. *J. Geophys. Res.* 103, 9713–9719.
- Brown, G.C., Mussett, A.E., 1981. *The Inaccessible Earth*. George Allen & Unwin, London, 235 pp.
- Cheng, W., Ganguly, J., 1994. Some aspects of multicomponent excess free energy models with subregular binaries. *Geochim. Cosmochim. Acta* 58, 3763–3767.
- Christensen, U., Yuen, D., 1984. The interaction of a subducting lithospheric slab with a chemical or phase boundary. *J. Geophys. Res.* 89, 4389–4402.
- Davies, G.F., 1999. *Dynamic Earth*, Cambridge, 458 pp.
- Dziewonski, A.M., Anderson, D.L., 1981. Preliminary reference earth model. *Phys. Earth Planet. Int.* 25, 297–356.
- Elkins, L.T., Grove, T.L., 1990. Ternary feldspar experiments and thermodynamic models. *Am. Miner.* 75, 544–559.
- Eriksson, G., Rosén, E., 1973. Thermodynamic studies of high temperature equilibria III. General equations for the calculation of equilibria in multiphase systems. *Thermochim. Scripta* 4, 193–194.
- Eriksson, G., 1975. Thermodynamic studies of high temperature equilibria XII. SOLGASMIX, a computer program calculation of equilibrium compositions in multiphase systems. *Chimica Scripta* 8, 100–103.
- Fabrichnaya, O., Saxena, S.K., Richet, P., Westrum, E.F., 2004. *Thermodynamic Data, Models, and Phase Diagrams in Multicomponent Oxide Systems*. Springer-Verlag.
- Fabrichnaya, O., 1999. The phase relations in the FeO – MgO – Al_2O_3 – SiO_2 system: assessment of thermodynamic properties and phase equilibria at pressures up to 30 GPa. *Calphad* 23, 19–67.
- Fabrichnaya, O., 1998. The assessment of thermodynamic properties for solid phases in the system FeO – MgO – O and FeO – MgO – Si – O systems. *Calphad* 22, 85–125.
- Fei, Y., Van Orman, J., Li, W., Van Westrenen, C., Sanloup, M., Minarik, K., Hirose, T., Komabayashi, M., Walter, K., Funakoshi, K., 2004. Experimentally determined postspinel transformation boundary in Mg_2SiO_4 using MgO as an internal pressure standard and its geophysical implications. *J. Geophys. Res.* 109, B02305, doi:10.1029/2003JB002562.
- Forsyth, D.W., Uyeda, S., 1975. On the relative importance of the driving forces of plate motion. *J. R. Astron. Soc.* 43, 163–200.
- Ganguly, J., Saxena, S.K., 1987. *Mixtures and Mineral Reactions*. Springer-Verlag, 291 pp.
- Ganguly, J., Cheng, W., Tirone, M., 1996. Thermodynamics of aluminosilicate garnet solid solution: new experimental data, an optimized model, and thermometric applications. *Contrib. Miner. Petrol.* 126, 137–151.
- Gasparik, T., 2000. Evidence for immiscibility in majorite garnet from experiments at 13–15 GPa. *Geochim. Cosmochim. Acta* 64, 137–151.
- Gasparik, T., 2003. *Phase Diagrams for Geoscientists*. Springer-Verlag.
- Grand, S.P., van der Hilst, R.D., Widiyantoro, S., 1997. Global seismic tomography: a snapshot of convection in the Earth. *GSA Today* 7, 1–7.
- Griffiths, R.W., Turner, J.S., 1998. Understanding mantle dynamics through mathematical models and laboratory experiments. In: Jackson, I. (Ed.), *The Earth's Mantle: Composition, Structure and Evolution*. Cambridge, UK, pp. 191–258.
- Hager, B.H., 1984. Subducted slabs and the geoid: constraints on mantle rheology and flow. *J. Geophys. Res.* 89, 6003–6015.
- Hillert, M., 1998. *Phase Equilibria, Phase Diagrams and Phase Transformations: Their Thermodynamic Basis*. Cambridge, UK, 538 pp.
- Hirose, K.Y., Fei, Y., Ma, Y., Mao, H.-K., 1999. The fate of subducted basaltic crust in the Earth's lower mantle. *Nature* 397, 53–56.
- Hirose, K., Takafuji, N., Sata, N., Ohishi, Y., 2005. Phase transition and density of subducted MORB crust in the lower mantle. *Earth Planet. Sci. Lett.* 237, 239–251.
- Hoffmann, A.W., White, W.M., 1982. Mantle plumes from ancient oceanic crust. *Earth Planet. Sci. Lett.* 57, 421–436.
- Holland, T.J.B., 1980. The reaction albite = jadeite + quartz determined experimentally in the range 600–1200 °C. *Am. Miner.* 65, 129–134.
- Iidaka, T., Suestuga, D., 1992. Seismological evidence of metastable olivine inside a subducting slab. *Nature* 356, 593–595.
- Irifune, I., Ringwood, A.E., 1993. Phase transformations in subducted oceanic crust and buoyancy relationships at depth of 600–800 km in the mantle. *Earth Planet. Sci. Lett.* 117, 101–110.

- Irifune, I., Nishiyama, N., Kuroda, K., Inoue, T., Isshiki, M., Utsumi, W., Funakoshi, K., Urakawa, S., Uchida, T., Katsura, T., Ohtaka, O., 1998. The post-spinel boundary in Mg_2SiO_4 determined by in situ X-ray diffraction. *Science* 279, 1700–1968.
- Ito, E., Takahashi, E., 1989. Post spinel transformations in the system Mg_2SiO_4 – Fe_2SiO_4 and some geophysical implications. *J. Geophys. Res.* 94, 10,637–10,646.
- Jiang, G., Zhao, D., Zhang, G., 2008. Seismic evidence for a metastable olivine wedge in the subducting Pacific slab under Japan sea. *Earth Planet. Sci. Lett.* 270, 300–307.
- Kaneshima, S., Okamoto, T., Takenaka, H., 2007. Evidence for metastable olivine wedge inside the subducted Mariana slab. *Earth Planet. Sci. Lett.* 258, 219–227.
- Katsura, T., Yamada, H., Shinmei, T., Kubo, A., Ono, S., Kanzaki, A., Yoneda, M.J., Walter, E., Ito, S., Urakawa, K., Funakoshi, W., Utsumi, W., 2003. Post-spinel transition in Mg_2SiO_4 determined by high P–T in situ X-ray diffraction. *Phys. Earth Planet. Int.* 136, 11–24.
- Kincaid, C., Olson, P., 1987. An experimental study of subduction and slab migration. *J. Geophys. Res.* 92, 13,832–13,840.
- Kirby, S.H., Stein, S., Okal, E.A., Rubie, D.C., 1996. Metastable mantle phase transformations and deep earthquakes in subducting oceanic lithosphere. *Rev. Geophys.* 34, 261–306.
- Kojitani, H., Navrotsky, A., Akaogi, M., 2001. Calorimetric study of perovskite solid solutions in the CaSiO_3 – CaGeO_3 system. *Phys. Chem. Miner.* 28, 413–420.
- Komabayashi, T., Omori, S., 2006. Internally consistent thermodynamic data set for dense hydrous magnesium silicates up to 35 GPa, 1600 °C: implications for water circulation in the Earth's deep mantle. *Phys. Earth Planet. Int.* 156, 89–107.
- Kubo, T., Ohtani, E., Kato, T., Urakawa, S., Suzuki, A., Kanbe, Y., Funakoshi, K.-I., Utsumi, W., Kikegawa, T., Fujino, K., 2002. Mechanism and kinetics of post-spinel transformation in Mg_2SiO_4 . *Phys. Earth Planet. Int.* 129, 153–171.
- Lawrence, J.F., Shearer, P.M., 2006. Constraining seismic velocity and density for the mantle transition zone with reflected and transmitted waveforms. *G3: Geochem. Geophys. Geosyst.* 7, Q10012, doi:10.1029/2006GC001339.
- Litasov, K., Ohtani, E., Sano, A., Suzuki, A., Funakoshi, K., 2005. In situ X-ray diffraction study of post-spinel transformation in a peridotite mantle: implication for the 660-km discontinuity. *Earth Planet. Sci. Lett.* 238, 311–328.
- Mosenfelder, J.L., Marton, F.C., Ross, C.R., Kerschhofer, L., Rubie, D.C., 2001. Experimental constraints on the depth of olivine metastability in subducting lithosphere. *Phys. Earth Planet. Int.* 127, 165–180.
- Murakami, M., Hirose, K., Kawamura, K., Sata, N., Ohishi, Y., 2004. Post-perovskite phase transition in MgSiO_3 . *Science* 304, 855–858.
- McKenzie, D.P., 1969. Speculation on the consequences and causes of plate motions. *Geophys. J. R. Astron. Soc.* 18, 1–32.
- Oganov, A.R., Ono, S., 2004. Theoretical and experimental evidence for a post-perovskite phase transformation of MgSiO_3 in the Earth's D' layer. *Nature* 430, 445–448.
- Palme, H., O'Neill, H.St.C., 2003. Cosmochemical estimates of mantle composition. In: R.W. Carlson (Ed.), *The Mantle and Core. Treatise in Geochemistry v. 2*, pp. 1–38.
- Ricard, Y., Mattern, E., Matas, J., 2005. Seismic tomographic images of slabs from mineral physics. In: van der Hilst, R.D., Bass, J.D., Matas, J., Trampert, J. (Eds.), *Earth's Deep Mantle: Structure, Composition and Evolution. Geophys. Monogr. Ser.*, vol. 160. Amer. Geophys. Union, pp. 283–300.
- Ringwood, A.E., 1994. Role of the transition zone and 660 km discontinuity in mantle dynamics. *Phys. Earth Planet. Int.* 86, 5–24.
- Ringwood, A.E., Irifune, I., 1988. Nature of the 650 km seismic discontinuity: implications for mantle dynamics and differentiation. *Nature* 331, 131–136.
- Ringwood, A.E., 1982. Phase transformations and differentiation in subducted lithosphere: Implications for mantle dynamics, basalt petrogenesis, and crustal evolution. *J. Geol.* 90, 611–643.
- Saikia, A., Frost, D.J., Rubie, D.C., Akaogi, M., Kojitani, H., 2007. A calorimetric study of $\text{Mg}_3(\text{Mg},\text{Si})\text{Si}_3\text{O}_{12}$ (majorite) and $\text{Mg}_3\text{Al}_2\text{Si}_4\text{O}_{12}$ (pyrope) garnet solid solution. Annual Report, Bayerisches Forschungsinstitut für Experimentelle Geochemie und Geophysik, Universität Bayreuth, pp. 94–96.
- Saxena, S.K., 1996. Earth mineralogical model: Gibbs free energy minimization computation in the system MgO – FeO – SiO_2 . *Geochim. Cosmochim. Acta* 60, 2379–2395.
- Saxena, S.K., Eriksson, G., 1983. Theoretical computation of mineral assemblages in pyrolyte and lherzolite. *J. Petrol.* 24, 538–555.
- Saxena, S.K., Eriksson, G., 1986. Chemistry of the formation of the terrestrial planets. In: S.K. Saxena (Ed.), *Chemistry and Physics of Terrestrial Planets. Adv. Phys. Geochem.* 6, 30–105.
- Saxena, S.K., Chatterjee, N., Fei, Y., Shen, G., 1993. *Thermodynamic Data on Oxides and Silicates*. Springer-Verlag, Heidelberg, 428 pp.
- Stein, C.A., Stein, S., 1992. A model for global variation in oceanic depth and heat flow with lithospheric age. *Nature* 359, 123–129.
- Stixrude, L., Lithgow-Bertelloni, C., Kiefer, B., Fumagalli, P., 2007. Phase stability in CaSiO_3 perovskite at high pressure. *Phys. Rev. B* 75, 04108–1–04108–10.
- Takahashi, E., 1986. Melting of a dry peridotite KLB-1 up to 14 GPa: implications on the origin of peridotitic upper mantle. *J. Geophys. Res.* 91, 9367–9382.
- Tetzlaff, M., Schmeling, H., 2000. The influence of olivine metastability on deep subduction of oceanic lithosphere. *Phys. Earth Planet. Int.* 120, 29–38.
- Toksöz, M.N., Sleep, N.H., Smith, A.T., 1973. Evolution of the downgoing lithosphere and the mechanisms of deep focus earthquakes. *Geophys. J. R. Astron. Soc.* 35, 285–310.
- Vacher, P., Mocquet, A., Sotin, C., 1998. Computation of seismic profiles from mineral physics: the importance of non-olivine components for explaining the 660 km discontinuity. *Phys. Earth Planet. Int.* 106, 275–298.
- van der Hilst, R., Engdahl, R., Spakman, W., Nolet, G., 1991. Tomographic imaging of subducted lithosphere below northwest Pacific island arcs. *Nature* 353, 37–43.
- Vinograd, V., Winkler, B., Putnis, A., Kroll, H., Milman, V., Gale, J.D., Fabricnaya, O.B., 2006. Thermodynamics of pyrope-majorite, $\text{Mg}_3\text{Al}_2\text{Si}_3\text{O}_{12}$ – $\text{Mg}_4\text{Si}_4\text{P}_{12}$, solid solution from atomistic model calculations. *Mol. Simulation* 32, 85–99.
- Weins, D.A., Gilbert, H.J., 1996. Effect of slab temperature on deep-earthquake aftershock productivity and magnitude-frequency relations. *Nature* 384, 153–156.
- Wood, B.J., 1979. Activity-composition relations in $\text{Ca}(\text{Mg},\text{Fe})\text{Si}_2\text{O}_6$ – $\text{CaAlSi}_2\text{O}_6$ clinopyroxene solid solutions. *Am. J. Sci.* 279, 854–875.